

# Light Confinement Effect Induced Highly Sensitive, Self-Driven Near-Infrared Photodetector and Image Sensor Based on Multilayer PdSe<sub>2</sub>/Pyramid Si Heterojunction

Feng-Xia Liang, Xing-Yuan Zhao, Jing-Jing Jiang, Ji-Gang Hu,\* Wei-Qiang Xie, Jun Lv,\* Zhi-Xiang Zhang, Di Wu, and Lin-Bao Luo\*

In this study, a highly sensitive and self-driven near-infrared (NIR) light photodetector based on PdSe<sub>2</sub>/pyramid Si heterojunction arrays, which are fabricated through simple selenization of predeposited Pd nanofilm on black Si, is demonstrated. The as-fabricated hybrid device exhibits excellent photoresponse performance in terms of a large on/off ratio of  $1.6 \times 10^5$ , a responsivity of  $456 \text{ mA W}^{-1}$ , and a high specific detectivity of up to  $9.97 \times 10^{13}$  Jones under 980 nm illumination at zero bias. Such a relatively high sensitivity can be ascribed to the light trapping effect of the pyramid microstructure, which is confirmed by numerical modeling based on finite-difference time domain. On the other hand, thanks to the broad optical absorption properties of PdSe<sub>2</sub>, the as-fabricated device also exhibits obvious sensitivity to other NIR illuminations with wavelengths of 1300, 1550, and 1650 nm, which is beyond the photoresponse range of Si-based devices. It is also found that the PdSe<sub>2</sub>/pyramid Si heterojunction device can also function as an NIR light sensor, which can readily record both “tree” and “house” images produced by 980 and 1300 nm illumination, respectively.

## 1. Introduction

Photodetectors are critical components of most modern optoelectronic systems, which find wide application in a variety of fields including image sensing, optical communication, industrial

automation, and medical diagnostics.<sup>[1–3]</sup> Up to now, a number of high-performance photodetectors with different geometries have been reported based on inorganic element and compound materials such as Si, GaAs, GaP, and InGaAs.<sup>[4,5]</sup> Among these semiconductors, Si is most widely employed, especially in complementary metal oxide semiconductor (CMOS) devices and advanced light detection systems.<sup>[6–8]</sup> In spite of the huge progress, it is undeniable that Si-based NIR photodetectors often suffer from relatively narrow wavelength photoresponse due to its cutoff around 1.1  $\mu\text{m}$ . To address this issue, various Ge, PbS, and HgCdTe semiconductors with bandgap much smaller than that of silicon have been introduced into silicon-based NIR photodetectors.<sup>[9–11]</sup> Although great efforts have been made in this field, these heterojunction photodetectors also have their own shortcomings. For example,

the fabrication of these semiconductor heterojunction usually entails the usage of very complicated methods such as molecular beam epitaxy (MBE) or metal–organic chemical vapor deposition (MOCVD),<sup>[10,11]</sup> leading to relatively high production cost. Thereby, the fabrication of low-cost and efficient Si-based infrared photodetectors with broadband sensitivity is still in great demand.

The rise of 2D semiconductors with unique atomic structure and excellent electronic properties provides an exciting opportunity for the building of electronic and optoelectronic devices. Graphene is the first discovered 2D materials that have gained tremendous attention due to its excellent electronic, optical, and mechanical properties.<sup>[12,13]</sup> However, the lack of inherent bandgap and short carrier lifetime has restricted its further application. Very recently, the transition metal dichalcogenides (TMDs) including MoS<sub>2</sub>, WS<sub>2</sub>, MoSe<sub>2</sub>, and WSe<sub>2</sub> complement the gapless graphene in that their bandgap is tunable from 1 to 2 eV.<sup>[14–17]</sup> In conjunction with the other appealing properties, such as high carrier mobility and wide light absorption, these 2D TMDs have been successfully applied in a variety of fields such as solar cells,<sup>[14]</sup> field-effect transistors,<sup>[16]</sup> and photodetectors.<sup>[17]</sup> In addition to the 2D TMDs mentioned above, the newly discovered group-10 TMDs, for example, PdSe<sub>2</sub>, have also been predicted to possess excellent electronic and optoelectronic properties. Take PdSe<sub>2</sub> for example, it has

Prof. F.-X. Liang, X.-Y. Zhao, J.-J. Jiang, Prof. J. Lv  
School of Material Science and Engineering and Anhui Provincial Key  
Laboratory of Advanced Functional Materials and Devices  
Hefei University of Technology  
Hefei 230009, China  
E-mail: lvjun@hfut.edu.cn

Dr. J.-G. Hu, W.-Q. Xie, Z.-X. Zhang, Prof. L.-B. Luo  
School of Electronic Science and Applied Physics  
Hefei University of Technology  
Hefei 230009, China  
E-mail: hujigang@hfut.edu.cn; luolb@hfut.edu.cn

Dr. D. Wu  
Key Laboratory of Materials Physics of Ministry of Education  
Department of Physics and Engineering  
Zhengzhou University  
Zhengzhou 450052, China

 The ORCID identification number(s) for the author(s) of this article can be found under <https://doi.org/10.1002/sml.201903831>.

DOI: 10.1002/sml.201903831

a narrower bandgap and larger bandgap tenability from monolayer (1.3 eV) to bulk (0 eV),<sup>[18]</sup> rendering it highly potential in infrared light detection devices. To date, there are only several reports on the investigation of PdSe<sub>2</sub>-based devices. For example, Xiao's group has extensively studied the unique pentagonal structure and electronic properties of the 2D PdSe<sub>2</sub> materials from mechanical exfoliation method. It is found that the few-layer PdSe<sub>2</sub> field-effect transistor device was very stable, with an electron field-effect mobility as high as 158 cm<sup>2</sup> V<sup>-1</sup> s<sup>-1</sup>, indicative of potential application for 2D electronics.<sup>[19]</sup> Hu's group has developed a long-wavelength infrared photodetector based on multilayer PdSe<sub>2</sub> single crystals with narrow bandgap less than 0.1 eV. The as-assembled multilayer PdSe<sub>2</sub> field-effect transistor device and 2D PdSe<sub>2</sub>-MoS<sub>2</sub> heterostructure photodetector exhibited apparent sensitivity to the wavelength of 10.6 μm infrared light, with a photoresponsivity of 42.1 A W<sup>-1</sup> and a specific detectivity of 8.21 × 10<sup>9</sup> Jones for each device, respectively.<sup>[20]</sup>

Enlightened by the above work, we here report a multilayer PdSe<sub>2</sub>/pyramid Si heterojunction array for broadband photodetection application. The proof-of-concept device was fabricated by directly selenizing Pd nanofilm on the surface of pyramid Si. Finite-difference time-domain (FDTD) modeling of the PdSe<sub>2</sub>/pyramid Si structure revealed that the incident light can be effectively trapped within the pyramid Si or at the PdSe<sub>2</sub>/Si interface, by virtue of the light trapping effect or resonant absorption. Further optoelectronic analysis finds that the PdSe<sub>2</sub>/pyramid Si device exhibits excellent photovoltaic properties under visible/NIR illuminations. Specifically, under 980 nm illumination the on/off ratio, responsivity, and specific detectivity are estimated to be 1.6 × 10<sup>5</sup>, 456 mA W<sup>-1</sup>, and 9.97 × 10<sup>13</sup> Jones, which surpasses most of the other Si-based infrared photodetectors. Moreover, owing to the broadband optical property of multilayer PdSe<sub>2</sub>, the hybrid device also displays

apparent photoresponse to longer infrared light (>1.1 μm). Finally, the capability of the as-fabricated photodetector for infrared light image sensors was also evaluated. The above result confirms that present multilayer PdSe<sub>2</sub>/pyramid Si photodetector may find promising application in future infrared optoelectronic devices and systems.

## 2. Results and Discussion

Figure 1a illustrates the structure of the proposed device composed of 3D wrapped multilayer PdSe<sub>2</sub>/pyramid Si heterojunction. The detailed device fabrication process is shown in Figure S1 (Supporting Information). Briefly, the pyramid Si was first prepared by alkaline etching of n-type lightly doped silicon wafer.<sup>[21–23]</sup> Afterward, a layer of 10 nm metal palladium was evaporated onto pyramid Si through electron beam evaporation, followed by a simple selenization process of Pd. Finally, multilayer PdSe<sub>2</sub>/pyramid Si device was deposited with Au and In/Ga electrodes on the two opposite sides, respectively. Figure S2 (Supporting Information) shows a typical camera picture of pyramid Si, Pd/pyramid Si, and PdSe<sub>2</sub>/pyramid Si. It was observed that the color gradually transformed from light gray to dark gray. The top-view field-effect scanning electron microscopy (FESEM) image of the PdSe<sub>2</sub> film on planar Si is displayed in Figure S3a (Supporting Information), which has a smooth surface with good continuity and compactness. Further energy-dispersive spectroscopy (EDS) in Figure S3b (Supporting Information) reveals that the film is composed of Pd and Se elements, with an atomic ratio close to 1:2. The film thickness of PdSe<sub>2</sub> on planar Si was measured through the atomic force microscope (AFM), which was estimated to be about 38 nm, as shown in Figure 1b. In fact, this thickness is about 3–4 times larger than that of Pd film. Additionally, the composition

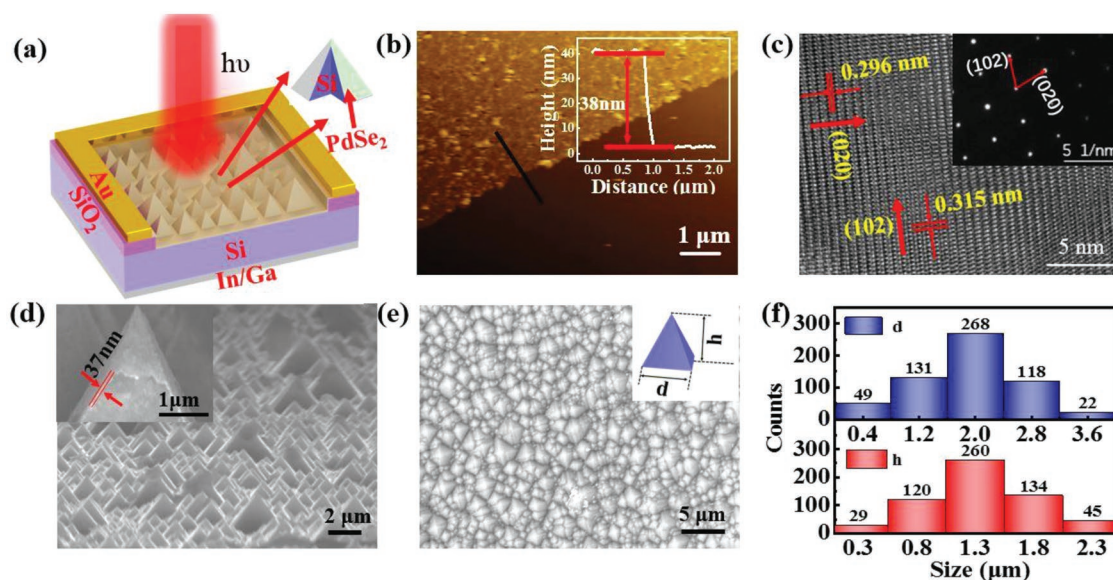


**Figure 1.** a) Schematic illustration of the PdSe<sub>2</sub>/pyramid Si heterojunction photodetector. b) AFM image of the PdSe<sub>2</sub> film on plane Si, the inset shows the height profile of PdSe<sub>2</sub> nanofilm. c) HRTEM image of the PdSe<sub>2</sub>, the inset shows the corresponding selected area electron diffraction pattern. d) A typical cross-sectional SEM image of PdSe<sub>2</sub>/pyramid Si. e) The bird-view of pyramid Si. f) The diameter and height distribution of pyramid Si.

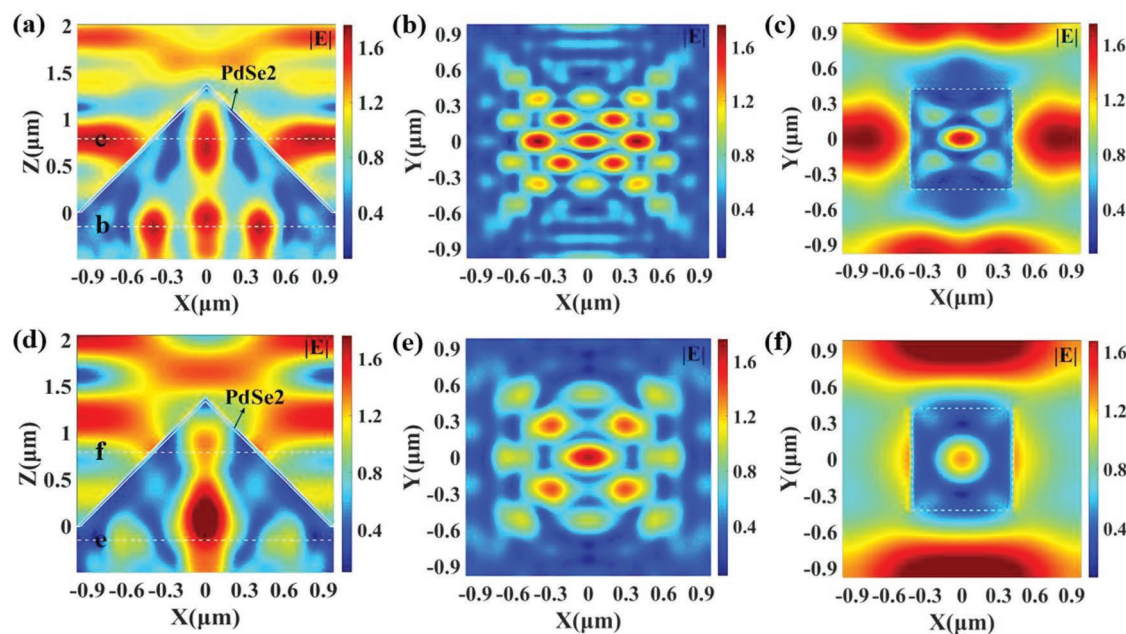


**Figure 2.** Simulation of electric field energy distribution of the PdSe<sub>2</sub>/pyramid Si with a wavelength of a–c) 980 nm and d–f) 1300 nm.

and structure of PdSe<sub>2</sub> were further confirmed through the Raman spectrum, X-ray diffraction (XRD), and X-ray photoelectron spectroscopy (XPS) in Figure S4 (Supporting Information). Raman spectrum shows four distinct peaks located at  $\approx 144$ ,  $\approx 206$ ,  $\approx 222$ , and  $\approx 255$  cm<sup>-1</sup>, which corresponds to A<sub>g</sub><sup>1</sup>, A<sub>g</sub><sup>2</sup>, B<sub>g</sub><sup>1</sup> movements modes of Se atoms and A<sub>g</sub><sup>3</sup> movement between Pd and Se atoms,<sup>[19,20]</sup> respectively (Figure S4a, Supporting Information). The XRD analysis affirms the structure of PdSe<sub>2</sub> phase in Figure S4b (Supporting Information), which possesses pentagonal structure with  $a = 5.75$ ,  $b = 5.87$ ,  $c = 7.69$  Å (PDF No. 11-0453). High-resolution transmission electron microscopy (HRTEM) was utilized to investigate the crystal structure of the as-prepared PdSe<sub>2</sub>. From the HRTEM image in Figure 1c, the 2D lattice fringe image can be easily observed. The  $d$ -spacing values in the image were calculated to be 0.296 and 0.315 nm, which can be attributed to the planes of (002) and (010).<sup>[20]</sup> Figure S4c,d (Supporting Information) shows the XPS measurement of PdSe<sub>2</sub> sample. Obviously, the two peaks at around 336.98 and 342.18 eV are in reference to the 3d<sub>5/2</sub> and 3d<sub>3/2</sub> spin-orbit peaks of Pd<sup>4+</sup>, while the other two peaks at 54.88 and 55.73 eV are attributed to 3d<sub>5/2</sub> and 3d<sub>3/2</sub> orbital of divalent Se<sup>2-</sup> ions.<sup>[18]</sup> The morphology of PdSe<sub>2</sub>/pyramid Si hybrid structure was then characterized by the SEM images in Figure 1d,e. It is found that the PdSe<sub>2</sub> film tightly wraps around the surface of the pyramid Si. The thickness of PdSe<sub>2</sub> on pyramid Si is measured to be about 37 nm, which is very close to the above AFM results. Figure 1f plots the statistical distribution of both bottom diameter and height of the pyramid Si, in which the bottom diameter of the pyramid Si ranges from 0.4 to 3.6 μm (average bottom diameter: 2.0 μm), while the height from 0.3 to 2.3 μm (average height: 1.3 μm).

The main reason for designing the above device configuration lies in the unique optical property of the PdSe<sub>2</sub>/pyramid Si array heterojunction. According to the effective medium theory,

pyramid or cone arrays could be treated as an effective dielectric film with a gradient refractive index along the negative direction of  $y$ -axis, which can significantly bridge the refractive index difference between bulk Si substrate and free space. As such, the guided mode can be excited by the incoming light over a broad spectral region, which may be confined at the different section of the pyramid Si, leading to the high absorption and strong light–matter interactions.<sup>[24]</sup> Figure 2a–c presents the electric field intensity distribution at different cross sections of this PdSe<sub>2</sub>/pyramid Si heterostructure under illumination with 980 nm, based on FDTD simulation. It was observed that the resonantly enhanced electric fields emerge not only inside the Si pyramid but also the silicon slab below. Moreover, it is also noted that electric fields are intensified in the gap between the neighboring pyramids. This signifies that the photons can be efficiently trapped either at the interface of PdSe<sub>2</sub>/pyramid Si or inside the Si, which could be eventually absorbed to generate carriers. The unique optical phenomenon is usually termed as light trapping effect<sup>[25]</sup> or resonant absorption,<sup>[26,27]</sup> which is highly beneficial for light detection. Please note that as the wavelength increases to 1300 nm (Figure 2d–f), a strong electric field could also be observed inside the pyramid Si. However, the pyramids Si can hardly absorb this longer wavelength as the photon energy is insufficient to generate the electron–hole pairs in the pyramids Si.

Figure 3a displays the digital photo of the as-fabricated device on PCB boards. The effective heterojunction area is about 0.02 cm<sup>2</sup>. To evaluate the capability of this device for NIR light detection, the photoresponse characteristics upon 980 nm illumination were investigated. Figure 3b depicts the  $I$ – $V$  curve in dark, from which a typical rectifying behavior with a rectification ratio of about 183 at the voltage of  $\pm 2$  V is observed. Since both Au/PdSe<sub>2</sub>/Au and In-Ga/Si/In-Ga are Ohmic contacts (Figure S5, Supporting Information), such a rectification

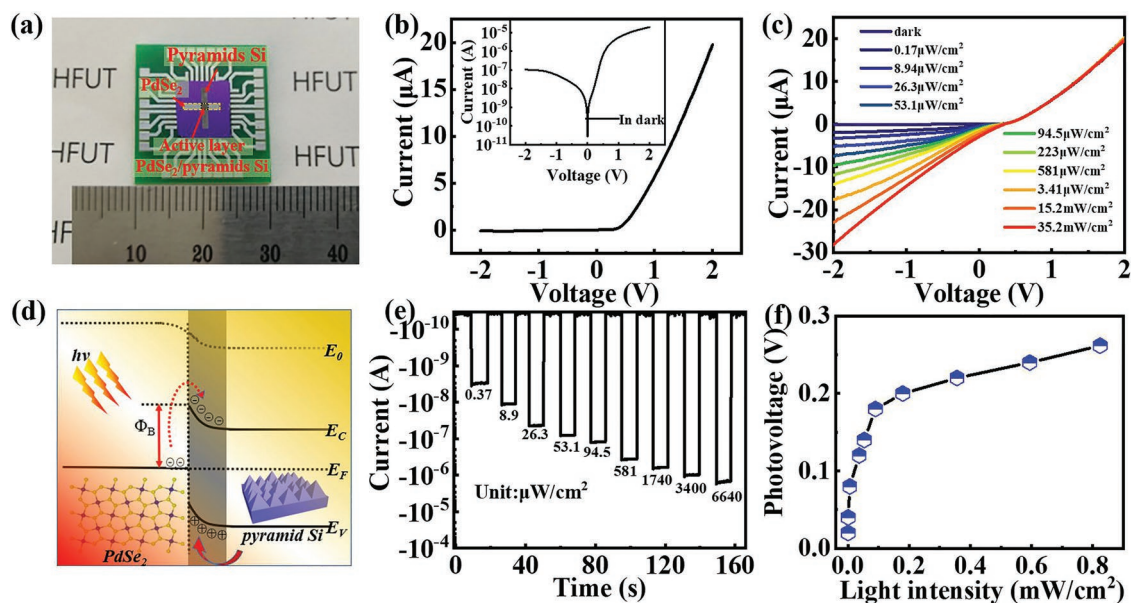


**Figure 3.** a) Digital photograph of the as-fabricated PdSe<sub>2</sub>/pyramid Si photodetector. b) *I*–*V* characteristics of the PdSe<sub>2</sub>/pyramid Si heterojunction in dark at room temperature, the inset shows the curve in a semilogarithmic scale. c) *I*–*V* curves of the PdSe<sub>2</sub>/pyramid Si photodetector under 980 nm light with different light intensities. d) Energy band diagram of the PdSe<sub>2</sub>/pyramid Si heterojunction under light illumination at zero bias. e) Photoresponse of the device under 980 nm light with various light intensities at zero bias. f) Photovoltage as a function of different light intensity.

behavior should stem from the PdSe<sub>2</sub>/pyramid Si interface. Furthermore, the photoresponse under different illumination intensities was studied. As can be seen from Figure 3c, when the light illumination increase gradually from 0.17 μW cm<sup>-2</sup> to 35.2 mW cm<sup>-2</sup>, the current at the reversed voltage increase accordingly whereas the current nearly keeps unchanged at forward voltage. Further careful examination of the *I*–*V* curves finds that device actually exhibits obvious photovoltaic property. Such photovoltaic characteristics could be explained using the energy band diagram in Figure 3d. Owing to the difference in work function of PdSe<sub>2</sub> and pyramid Si, a built-in electric field or depletion layer could form at their interface, with the direction pointing from pyramid Si to PdSe<sub>2</sub>.<sup>[28]</sup> Upon light illumination, the photogenerated carriers from PdSe<sub>2</sub> and pyramid Si could be rapidly separated in the depletion layer, flowing to opposite sides and eventually forming photocurrent or photovoltage in the circuit.<sup>[29]</sup> During this photodetection process, the photocurrent and photovoltage are largely determined by the incident light intensity. With increasing light illumination, both short-circuit current and open-circuit voltage are found to increase accordingly, as revealed by Figure 3e,f.

To shed light on the dependence of photocurrent on light intensities of the heterojunction photodetector, the evolution of the photocurrent under different light intensities was then studied and plotted in Figure 4a. Obviously, the above dependence can be described by a power law of  $I = AP^\theta$ , where *I* is the photocurrent, *P* is light intensity, and  $\theta$  is an exponent determining the response of photocurrent to NIR intensity. Through fitting the curves at two different regions (low light intensity from 1.71 to 223 μW cm<sup>-2</sup> and high light intensity from 581 μW cm<sup>-2</sup> to 35.2 mW cm<sup>-2</sup>), two  $\theta$  values of 0.93 and 0.67 are obtained, respectively. These two exponents that deviate from the ideal value ( $\theta = 1$ ) suggest recombination loss during the

photodetection process. What's more, the relatively small  $\theta$  at high intensity is reasonable as higher density of the photo-generated carriers could be produced at stronger light intensities, which will lead to larger chance for carrier recombination.<sup>[30,31]</sup> It is also observed that both dark current and photocurrent monotonically decrease as the bias voltage gradually decreases (Figure 4b). Specifically, the corresponding on/off ratio (photocurrent/dark current) of the device reaches the highest value of  $1.6 \times 10^5$  at 0 V, and will decrease gradually to 128 when the bias voltage is decreased to -6 V, which is due to the relatively fast increase in dark current compared to the dark current.

To quantitatively assess the photoresponse of the present PdSe<sub>2</sub>/pyramid Si photodetector for 980 nm NIR detection, *R* and external quantum efficiency (EQE) were then calculated using the following two equations<sup>[32,33]</sup>

$$R = \frac{(I_\lambda - I_d)}{P_\lambda A} \quad (1)$$

$$\text{EQE} = R \frac{hc}{e\lambda} \quad (2)$$

Here, *R* represents the responsivity, which can be figured out by the following parameters of photocurrent (*I*<sub>λ</sub>), dark current (*I*<sub>d</sub>), power density (*P*<sub>λ</sub>), and active area of the device (*A*) as described in Equation (1). EQE indicates the number of effective carriers produced per incident photon. It can be calculated by Equation (2), where *h*, *c*, and  $\lambda$  are the Planck constant, light speed, and wavelength, respectively. Figure 4d,e plots the evolution of *R*, EQE, and on/off ratio with varying light intensities. Notably, except the on/off ratio, both *R* and EQE are found to decrease gradually as light intensity increases. Specifically, at a weak intensity of 0.171 μW cm<sup>-2</sup>, the *R* and EQE will reach the

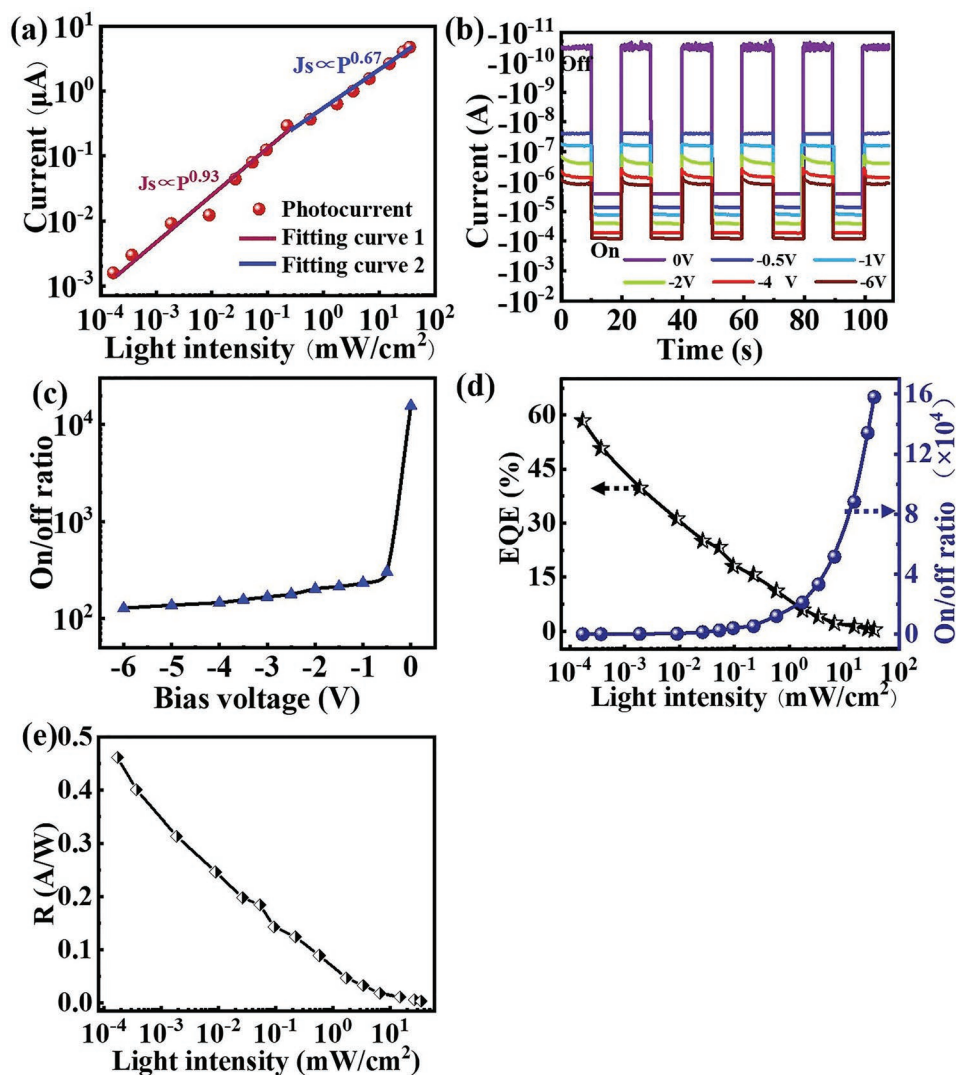


**Figure 4.** a) Photocurrents as a function of incident light intensity at zero bias. b) Time-dependent photoresponse of the device under 980 nm light illumination ( $15.23 \text{ mW cm}^{-2}$ ) at bias voltage of 0, -0.5, -1, -2, -4, and -6 V. c) On/off ratio of the device as a function of different bias voltages. d) On/off ratio and EQE of the device as a function of the light intensity at zero bias. e) The dependence of responsivity on light intensity at zero bias.

maximum values of  $456 \text{ mA W}^{-1}$  and 58%, respectively (Please refer to the Supporting Information for the detailed calculation of our device).

Besides the relatively high on/off ratio and  $R$ , the PdSe<sub>2</sub>/pyramid Si photodetector also exhibits a broadband sensitivity to illumination with wavelengths ranging from 300 to 1650 nm, which is beyond that of Si-based devices. In order to facilitate the study of spectral photoresponse in different wavelengths, another important metric, specific detectivity ( $D^*$ ) which is often used to evaluate the ability of detecting weak optical signal from noise was calculated by using the noise equivalent power from the following equations<sup>[34–36]</sup>

$$D^* = \frac{(A\Delta f)^{1/2}}{\text{NEP}} \quad (3)$$

$$\text{NEP} = \frac{i_n^{-1/2}}{R} \quad (4)$$

where  $A$ ,  $\Delta f$ , and  $i_n^{-1/2}$  are the effective area of the proposed device ( $0.02 \text{ cm}^2$ ), bandwidth, and root-mean-square value of the noise current, respectively. As presented in Figure 5a, the  $i_n^{-1/2}$  was obtained by directly recording the noise current of the device at different frequencies via a lock-in preamplifier in dark.<sup>[28,37]</sup> With regard to the calculation of  $D^*$ , the noise level of  $i_n^{-1/2}$  was extracted at the frequency of 1 Hz, which was about  $6.4 \times 10^{-13} \text{ A Hz}^{-1/2}$ . Figure 5b displays the evolution of both  $R$  and  $D^*$  as a function of wavelength. Apparently, both metrics will reach the highest values of  $0.456 \text{ A W}^{-1}$  and  $9.97 \times 10^{13} \text{ Jones}$ , respectively, when the wavelength is around 980 nm, which means the peak photosensitivity of this heterojunction device at around 980 nm. Table 1 compares the main parameters of this heterojunction photodetector and other Si-based devices with similar configurations. Even though the responsivity, on/off ratio, and specific detectivity are slightly lower than the device composed of SnSe/Si heterostructure,<sup>[38]</sup> these two parameters are much better than other silicon and silicon nanowire based

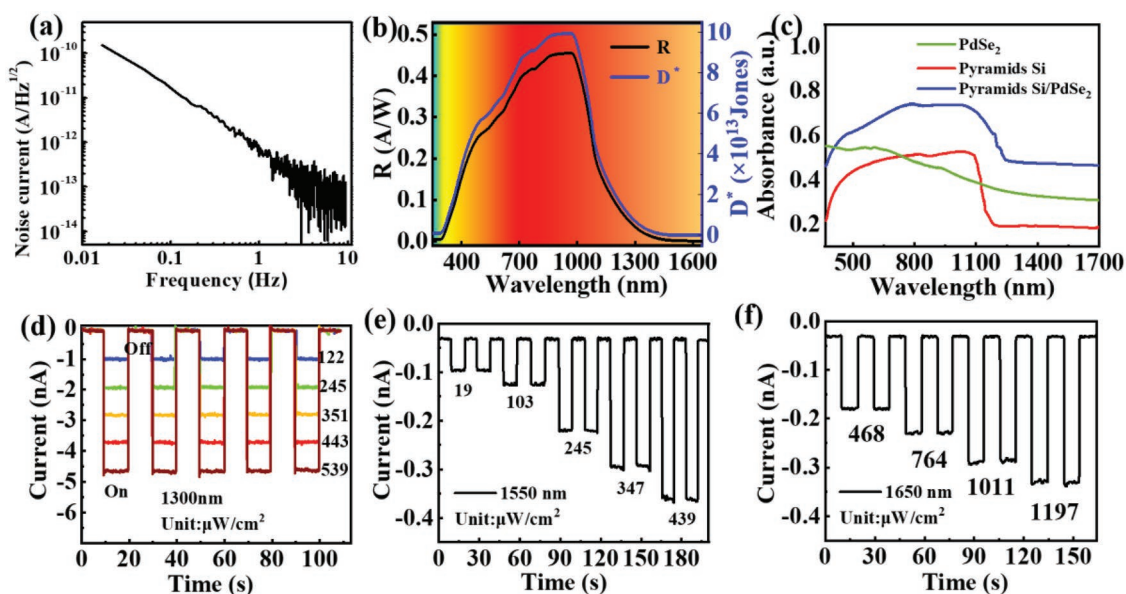


**Figure 5.** a) Noise current of the device at different frequency. b) Wavelength-dependent responsivity and specific detectivity of the device (from 300 to 1650 nm). c) UV–vis–NIR absorption spectra of PdSe<sub>2</sub>, the pyramid Si, and the PdSe<sub>2</sub>/pyramid Si. d–f) Photoresponse of the PdSe<sub>2</sub>/pyramid Si light with different light intensities under 1300, 1550, and 1650 nm, respectively.

devices including MoO<sub>3-x</sub>/pyramid Si,<sup>[39]</sup> graphene/Si,<sup>[40,41]</sup> a-C/Si,<sup>[42]</sup> CuO/Si NWs,<sup>[43]</sup> and even PtSe<sub>2</sub>/Si heterojunction.<sup>[44]</sup> This relatively good photoresponse property is mainly attributed to the special absorption properties of multilayer PdSe<sub>2</sub>/pyramid Si heterojunction. Figure 5c compares the absorption spectra of multilayer PdSe<sub>2</sub>, pyramid Si, and multilayer PdSe<sub>2</sub>/pyramid Si in UV–vis–NIR region. Obviously, once covered with multilayer PdSe<sub>2</sub>, the resultant multilayer PdSe<sub>2</sub>/pyramid Si hybrid structure will exhibit the strongest light absorption. More importantly, it is found that the multilayer PdSe<sub>2</sub> could also extend the light absorption range to 1.1 μm, the cutoff of Si (bandgap, 1.1 eV). In light of this, we further investigated the photoresponse of the PdSe<sub>2</sub>/pyramid Si hybrid device at other longer wavelengths. The typical photocurrent switching performance under different light intensities is shown in Figure 5d–f. It is found that apparent photoresponse is achieved at 1300, 1550, and 1650 nm. More concretely,  $D^*$  is obtained to be  $1.2 \times 10^{11}$  Jones for wavelength of 1300 nm,  $1.1 \times 10^{10}$  Jones for 1550 nm, and  $1.7 \times 10^{10}$  Jones for 1650 nm, respectively. Figure S6 (Supporting Information) depicts the temporal photoresponse in

1300 nm over 1000 switching cycles, which indicates that the photoresponse is highly reproducible, with very good stability.

As an important optoelectronic device, infrared image sensor has been widely applied in missile warning system, fire monitoring, camera, and fax machines.<sup>[45,46]</sup> To explore the possibility of the PdSe<sub>2</sub> film/pyramid Si heterojunction device for photosensing application, two NIR images of “house” and “tree” were obtained by shining a mask with a 980 or 1300 nm light source. The schematic diagram of the setup is depicted in Figure 6a, in which the individual device that is controlled by an automatic displacement platform was used to sense the image in Figure 6b. During the image sensing process, the PdSe<sub>2</sub> film/pyramid Si device will automatically collect the current of each pixel by scanning in the image, after which all the current will be collected by the 2D contrast current mapping software. Figure 6c,d shows the “house” and “tree” images projected by infrared light with wavelengths of 980 and 1300 nm, respectively. It is clear that the positions with the incident light passing through displays higher photocurrent, while the positions blocked by the image pattern exhibit lower current values.

**Table 1.** Comparison of key parameters of the present IRPD and other similar devices.

Device	$R$ [mA W <sup>-1</sup> ]	$D^*$ [Jones]	On/off ratio	Wavelength [nm]	Ref.
SnSe/Si	566.4	$4.4 \times 10^{12}$	$4.9 \times 10^5$	850 ( $V = 0$ V)	[38]
MoO <sub>3-x</sub> /pyramid Si	≈55	$6.29 \times 10^{12}$	–	850 ( $V = 0$ V)	[39]
Graphene/Si	29	$3.9 \times 10^{11}$	≈10 <sup>2</sup>	850 ( $V = 0$ V)	[40]
Bilayer graphene/Si	14	$5 \times 10^{12}$	≈10	980 ( $V = 0$ V)	[41]
3L graphene/Si	435	$7.69 \times 10^9$	≈10 <sup>2</sup>	885 ( $V = -2$ V)	[42]
CuO/Si NW array	29	$3.9 \times 10^{11}$	≈10 <sup>2</sup>	1064 ( $V = 0$ V)	[43]
PtSe <sub>2</sub> /Si	490	–	$3 \times 10^2$	970 ( $V = -2$ V)	[44]
PdSe <sub>2</sub> /pyramid Si	456	$9.97 \times 10^{13}$	$1.6 \times 10^5$	980 ( $V = 0$ V)	This work

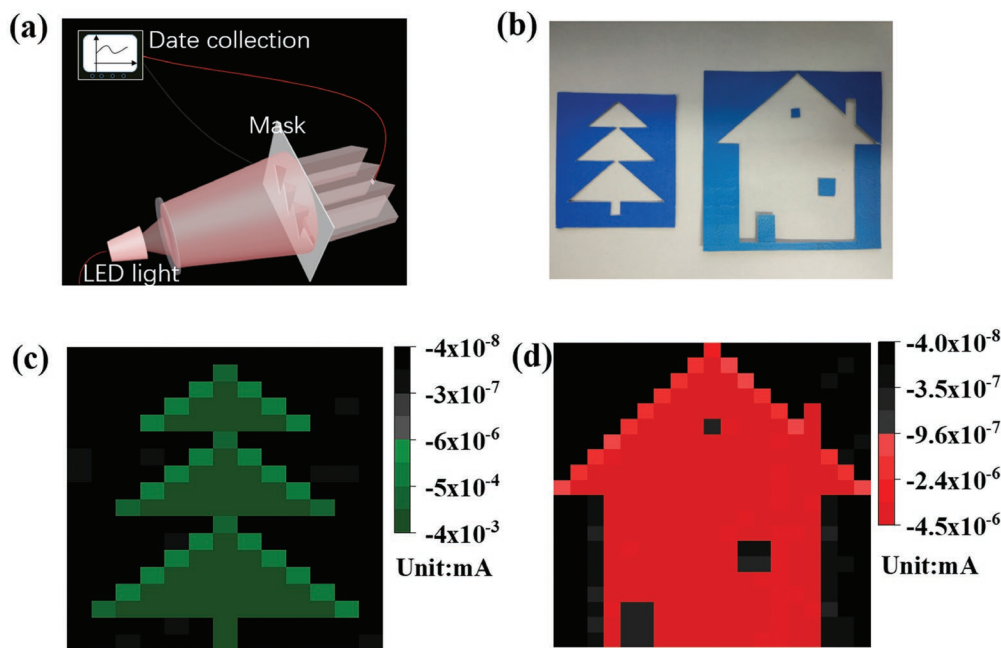


**Figure 6.** a) Schematic diagram of the setup for infrared image sensing. b) Digital photograph of the template “tree” and “house.” c,d) The corresponding 2D current mapping of image tree under 980 nm illumination and house under 1300 nm illumination, respectively.

Remarkably, the photocurrent of the device in the majority of the images has relatively uniform distribution, with an average value of  $4 \times 10^{-6}$  A for tree (980 nm) and  $4.5 \times 10^{-9}$  A for the house (1330 nm), respectively. Although there are some unfavorable regions, both tree and house NIR images could be easily distinguished from the background with satisfying resolution, indicating the great potential of our photodetector for reliable application in NIR image sensing.

### 3. Conclusions

In summary, we report a high-performance NIR photodetector based on PdSe<sub>2</sub>/pyramid Si heterojunction. The as-fabricated hybrid device exhibits apparent photovoltaic characteristics under NIR illumination, rendering it a self-driven device without power supply. Optoelectronic analysis reveals that this device displays pronounced photoresponse to 980 nm illumination, with the responsivity, specific detectivity, and EQE of 456 mA W<sup>-1</sup>,  $9.97 \times 10^{13}$  Jones, and 58%, respectively, which is much better than other devices with similar geometries. According to the FDTD simulation, this excellent device performance is associated with the strong light trapping effect of the pyramid structure. Besides, due to the absorption of PdSe<sub>2</sub>, the present heterojunction device is also capable of detecting longer infrared light of 1300, 1550, and 1650 nm. Finally, image sensors with PdSe<sub>2</sub>/pyramid Si photodetector were also fabricated, which demonstrated good ability in capturing the still images under 980 and 1300 nm illumination. The above result confirms that the present self-powered photodetector may be potential significant for future NIR optoelectronic devices and systems.

### 4. Experimental Section

**Materials Fabrication and Device Assembly:** The pyramid Si was synthesized through a simple alkali etching method. First, n-type lightly doped (100) Si wafer ( $1-10 \Omega \text{ cm}^{-1}$ ) with 300 nm thick SiO<sub>2</sub> insulating layer was ultrasonicated sequentially in ethanol, acetone, and deionized water. Afterward, an open window of  $1.4 \times 6$  mm was formed by photolithography method, followed by the etching of SiO<sub>2</sub> insulator layer in buffered oxide etch (BOE, 30 wt% HF:NH<sub>4</sub>F:H<sub>2</sub>O = 3 mL:5 g:7 mL). Si pyramid array was then formed through anisotropic etching in an aqueous solution consisting of 5.0 wt% sodium hydroxide and 5.0 vol% isopropanol. The alkali etching was maintained at 80 °C for 40 min. Finally, the textured Si substrate was immersed in diluted hydrochloric acid to neutralize the residual NaOH before use. The PdSe<sub>2</sub> film was grown on top of the as-synthesized pyramid Si in a crossing way. In brief, an open window ( $1.4 \times 6$  mm) across pyramid Si was obtained through the same photolithography method, on which Pd film with the thickness of 8 nm was deposited via electron beam evaporation. The as-grown Pd/pyramid Si was then mounted at the center zone of the furnace, while selenium powder (99.99%) was placed upstream. During the selenization process, the heating temperature of selenium powder was set to 700 K for 1 h with the carrier gas of Ar and H<sub>2</sub> controlled at 50 sccm. To fabricate the multilayer PdSe<sub>2</sub>/pyramid Si photodetector, Au electrodes with a thickness of  $\approx 50$  nm were deposited on top of the as-selenized PdSe<sub>2</sub> by electron-beam deposition, while In–Ga alloy was pasted on the rear side of the Si substrate as the bottom electrode.

**Structural Analysis and Device Characterization:** The morphology of the as-fabricated PdSe<sub>2</sub>, pyramid Si, and multilayer PdSe<sub>2</sub>/pyramid Si films was characterized by FESEM (SU8020) and AFM (Benyuan Nanotech Com, CSPM-4000). The crystal structures of PdSe<sub>2</sub> film were analyzed by XRD (Rigaku D/max-rB) and HRTEM (JEM-2100F). Raman spectra of PdSe<sub>2</sub> were performed on a Raman spectrometer (Horiba Jobin Yvon, LabRAM HR800). The chemical composition of the PdSe<sub>2</sub> film was analyzed using EDS (SU8020) and XPS (ESCALAB250Xi). The absorption of the film was performed on a UV–vis spectrophotometer (UV-2550, Shimadzu, Japan). The electrical and optical characteristics of the as-fabricated device were measured using a semiconductor

characterization system (Keithley 2400) and different laser diodes with wavelengths of 980 nm (Tanon Company, UV-100), 1300 nm (Thorlabs, M1300L3), 1550 nm (Thorlabs, M1550L3), and 1650 nm (Thorlabs, M1650L3). The power intensity of all light sources was carefully calibrated through a power meter (Thorlabs GmbH, PM 100D) before measurement. All measurements were performed in air at room temperature.

**Theoretical Simulation:** FDTD method was adopted to calculate the electric field distribution of the 3D wrapped heterojunction structure. For modeling, the structural parameters of the heterojunction including bottom diameter and height were collected from the SEM image of the experimental sample. In this work, *x*-direction period (*P<sub>x</sub>*), *y*-direction period (*P<sub>y</sub>*), height (*H*) of pyramid Si, and thickness (*t*) of the PdSe<sub>2</sub> film were set to be 1.91 μm, 1.91 μm, 1.34 μm, and 38 nm, respectively. The periodic boundary conditions were applied in horizontal direction to simulate an infinite area, and the perfectly matched layer (PML) boundary conditions were set on the top/bottom sides. The dielectric constants of Si and PdSe<sub>2</sub> were chosen from previous work.<sup>[47,48]</sup>

## Supporting Information

Supporting Information is available from the Wiley Online Library or from the author.

## Acknowledgements

This work was supported by the National Natural Science Foundation of China (NSFC, Nos. 61575059, 61675062, 21501038), the Fundamental Research Funds for the Central Universities (JZ2018HGXC0001), the Open Foundation of Anhui Provincial Key Laboratory of Advanced Functional Materials and Devices (4500-411104/011), and Guangxi Key Laboratory for Electrochemical Energy Materials.

## Conflict of Interest

The authors declare no conflict of interest.

## Keywords

2D materials, black silicon, light manipulation, near-infrared light, optoelectronic devices

Received: July 17, 2019

Revised: August 23, 2019

Published online: September 12, 2019

- [1] W. Q. Wu, X. D. Wang, X. Han, Z. Yang, G. Y. Gao, Y. F. Zhang, J. F. Hu, Y. W. Tan, A. L. Pan, C. F. Pan, *Adv. Mater.* **2019**, *31*, 1805913.
- [2] T. Mueller, F. N. Xia, P. Avouris, *Nat. Photonics* **2010**, *4*, 297.
- [3] X. Gong, M. H. Tong, Y. J. Xia, W. Z. Cai, J. S. Moon, Y. Cao, G. Yu, C. L. Shieh, B. Nilsson, A. J. Heeger, *Science* **2009**, *325*, 1665.
- [4] Y. C. Tang, Z. Wang, P. Wang, F. Wu, Y. M. Wang, Y. F. Chen, H. L. Wang, M. Peng, C. X. Shan, Z. H. Zhu, S. Q. Qin, W. D. Hu, *Small* **2019**, *15*, 1805545.
- [5] Y. C. Tang, F. Wu, F. S. Chen, Y. Zhou, P. Wang, M. S. Long, W. J. Zhou, Z. J. Ning, J. W. He, F. Gong, Z. H. Zhu, S. Q. Qin, W. D. Hu, *Small* **2018**, *14*, 1803158.
- [6] R. An, B. M. Zhang, L. L. Han, X. D. Wang, Y. L. Zhang, L. Y. Shi, R. Ran, *J. Mater. Sci.* **2019**, *54*, 8515.
- [7] M. F. Peng, Y. J. Wang, Q. Q. Shen, X. K. Xie, H. C. Zheng, W. L. Ma, Z. Wen, X. H. Sun, *Sci. China Mater.* **2018**, *62*, 225.
- [8] V. Dhyani, P. Dwivedi, S. Dhanekar, S. Das, *Appl. Phys. Lett.* **2017**, *111*, 191107.
- [9] C. Y. Huang, D. Y. Wang, C. H. Wang, Y. T. Wang, Y. T. Jiang, Y. J. Yang, C. C. Chen, Y. F. Chen, *J. Phys. D: Appl. Phys.* **2011**, *44*, 085103.
- [10] L. He, J. R. Yang, S. L. Wang, Y. Wu, W. Z. Fang, *Adv. Mater.* **1999**, *11*, 1115.
- [11] W. E. Hoke, P. J. Lemonias, *Appl. Phys. Lett.* **1985**, *46*, 398.
- [12] S. Yang, M. R. Lohe, K. Mullen, X. Feng, *Adv. Mater.* **2016**, *28*, 6213.
- [13] H. H. Kim, Y. Chung, E. Lee, S. K. Lee, K. Cho, *Adv. Mater.* **2014**, *26*, 3213.
- [14] M. L. Tsai, M. Y. Li, J. R. D. Retamal, K. T. Lam, Y. C. Lin, K. Suenaga, L. J. Chen, G. Liang, L. J. Li, J. H. He, *Adv. Mater.* **2017**, *29*, 1701168.
- [15] K. K. H. Smithe, C. D. English, S. V. Suryavanshi, E. Pop, *Nano Lett.* **2018**, *18*, 4516.
- [16] T. F. Yang, B. Y. Zheng, Z. Wang, T. Tao, C. Pan, J. Zou, X. H. Zhang, Z. Y. Qi, H. J. Liu, Y. X. Feng, W. D. Hu, F. Miao, L. T. Sun, X. F. Duan, A. L. Pan, *Nat. Commun.* **2017**, *8*, 1096.
- [17] K. A. Zhang, T. N. Zhang, G. H. Cheng, T. X. Li, S. X. Wang, W. Wei, X. H. Zhou, W. W. Yu, Y. Sun, P. Wang, D. Zhang, C. G. Zeng, X. J. Wang, W. D. Hu, H. J. Fan, G. Z. Shen, X. Chen, X. F. Duan, K. Chang, N. Dai, *ACS Nano* **2016**, *10*, 3852.
- [18] W. L. Chow, P. Yu, F. Liu, J. Hong, X. Wang, Q. Zeng, C. H. Hsu, C. Zhu, J. Zhou, X. Wang, J. Xia, J. Yan, Y. Chen, D. Wu, T. Yu, Z. Shen, H. Lin, C. Jin, B. K. Tay, Z. Liu, *Adv. Mater.* **2017**, *29*, 1602969.
- [19] A. D. Oyedele, S. Yang, L. Liang, A. A. Puzos, K. Wang, J. Zhang, P. Yu, P. R. Pudasaini, A. W. Ghosh, Z. Liu, C. M. Rouleau, B. G. Sumpter, M. F. Chisholm, W. Zhou, P. D. Rack, D. B. Geohegan, K. Xiao, *J. Am. Chem. Soc.* **2017**, *139*, 14090.
- [20] M. S. Long, Y. Wang, P. Wang, X. H. Zhou, H. Xia, C. Luo, S. Y. Huang, G. W. Zhang, H. G. Yan, Z. Y. Fan, X. Wu, X. S. Chen, W. Lu, W. D. Hu, *ACS Nano* **2019**, *13*, 2511.
- [21] H. Y. Chen, H. L. Lu, Q. H. Ren, Y. Zhang, X. F. Yang, S. J. Ding, D. W. Zhang, *Nanoscale* **2015**, *7*, 15142.
- [22] P. Singh, S. K. Srivastava, M. Yameen, B. Sivaiah, V. Prajapati, P. Prathap, S. Laxmi, B. P. Singh, Vandana, C. M. S. Rauthan, P. K. Singh, *J. Mater. Sci.* **2015**, *50*, 6631.
- [23] P. Xiao, J. Mao, K. Ding, W. L. Luo, W. D. Hu, X. J. Zhang, X. H. Zhang, J. S. Jie, *Adv. Mater.* **2018**, *30*, 1801729.
- [24] E. Garnett, D. P. Yang, *Nano Lett.* **2010**, *10*, 1082.
- [25] K. X. Wang, Z. Yu, V. Liu, Y. Cui, S. Fan, *Nano Lett.* **2012**, *12*, 1616.
- [26] T. Nishihara, Y. Yamada, M. Okano, Y. Kanemitsu, *J. Phys. Chem. C* **2015**, *119*, 28654.
- [27] L. Cao, B. Nabet, J. E. Spanier, *Phys. Rev. Lett.* **2006**, *96*, 157402.
- [28] L. B. Luo, D. Wang, C. Xie, J. G. Hu, X. Y. Zhao, F. X. Liang, *Adv. Funct. Mater.* **2019**, *29*, 1900849.
- [29] Q. S. Lv, F. G. Yan, X. Wei, K. Y. Wang, *Adv. Opt. Mater.* **2018**, *6*, 1700490.
- [30] R. R. Zhuo, L. H. Zeng, H. Y. Yuan, D. Wu, Y. G. Wang, Z. F. Shi, T. T. Xu, Y. T. Tian, X. J. Li, Y. H. Tsang, *Nano Res.* **2018**, *12*, 183.
- [31] C. Xie, X. T. Lu, X. W. Tong, Z. X. Zhang, F. X. Liang, L. Liang, L. B. Luo, Y. C. Wu, *Adv. Funct. Mater.* **2019**, *29*, 1806006.
- [32] L. H. Zeng, M. Z. Wang, H. Hu, B. Nie, Y. Q. Yu, C. Y. Wu, L. Wang, J. G. Hu, C. Xie, F. X. Liang, L. B. Luo, *ACS Appl. Mater. Interfaces* **2013**, *5*, 9362.
- [33] D. Wu, Y. G. Wang, L. H. Zeng, C. Jia, E. P. Wu, T. T. Xu, Z. F. Shi, Y. T. Tian, X. J. Li, Y. H. Tsang, *ACS Photonics* **2018**, *5*, 3820.
- [34] R. C. Lin, W. Zheng, D. Zhang, Z. J. Zhang, Q. X. Liao, L. Yang, F. Huang, *ACS Appl. Mater. Interfaces* **2018**, *10*, 22419.
- [35] D. X. Guo, X. F. Wang, H. U. Wang, W. D. Song, H. Chen, M. Y. Qi, X. J. Luo, X. Luo, G. Li, G. G. Qin, S. T. Li, *ACS Photonics* **2018**, *5*, 4810.

- [36] Y. Y. Wang, Y. D. Wu, W. Peng, Y. H. Song, B. Wang, C. Y. Wu, Y. Lu, *Nanoscale* **2018**, *10*, 18502.
- [37] W. Deng, L. M. Huang, X. Z. Xu, X. J. Zhang, X. C. Jin, S. T. Lee, J. S. Jie, *Nano Lett.* **2017**, *17*, 2482.
- [38] L. Z. Hao, Z. G. Wang, H. Y. Xu, K. Y. Yan, S. C. Dong, H. Liu, Y. J. Du, Y. P. Wu, Y. J. Liu, M. D. Dong, *2D Mater.* **2019**, *6*, 034004.
- [39] C. X. Zhao, Z. M. Liang, M. Z. Su, P. Y. Liu, W. J. Mai, W. G. Xie, *ACS Appl. Mater. Interfaces* **2015**, *7*, 25981.
- [40] P. Lv, X. J. Zhang, X. W. Zhang, W. Deng, J. S. Jie, *IEEE Electron Device Lett.* **2013**, *34*, 1337.
- [41] L. Wang, S. J. He, K. Y. Wang, H. H. Luo, J. G. Hu, Y. Q. Yu, C. Xie, C. Y. Wu, L. B. Luo, *Nanotechnology* **2018**, *29*, 505203.
- [42] X. H. An, F. Z. Liu, Y. J. Jung, S. Kar, *Nano Lett.* **2013**, *13*, 909.
- [43] Q. Hong, Y. Cao, J. Xu, H. Lu, J. He, J. L. Sun, *ACS Appl. Mater. Interfaces* **2014**, *6*, 20887.
- [44] C. Yim, N. McEvoy, S. Riazimehr, D. S. Schneider, F. Gity, S. Monaghan, P. K. Hurley, M. C. Lemme, G. S. Duesberg, *Nano Lett.* **2018**, *18*, 1794.
- [45] Z. Sun, Z. Liu, J. Li, G. A. Tai, S. P. Lau, F. Yan, *Adv. Mater.* **2012**, *24*, 5878.
- [46] A. Rogalski, J. Antoszewski, L. Faraone, *J. Appl. Phys.* **2009**, *105*, 091101.
- [47] T. K. Chong, J. Wilson, S. Mokkalapati, K. R. Catchpole, *J. Opt.* **2012**, *14*, 024012.
- [48] S. Deng, L. Li, Y. Zhang, *ACS Appl. Nano Mater.* **2018**, *1*, 1932.